Multichannel Polarization-Controllable Superpositions of Orbital Angular Momentum States

Submitted to ADVANCED MATERIALS
DOI: 10.1002/adma.((please add manuscript number))
Article type: communications

Multichannel Polarization-Controllable Superpositions of Orbital Angular Momentum States

Fuyong Yue, Dandan Wen, Chunmei Zhang, Brian D. Gerardot, Wei Wang, Shuang Zhang, Xianzhong Chen**

F. Yue, D. Wen, C. Zhang, Prof. B. D. Gerardot, Dr. W. Wang, Dr. X. Chen
SUPA, Institute of Photonics and Quantum Sciences, School of Engineering and Physical Sciences, Heriot-Watt University, Edinburgh, EH14 4AS, UK
E-mail: x.chen@hw.ac.uk
Prof. S. Zhang
School of Physics and Astronomy, University of Birmingham, B15 2TT, UK
E-mail: s.zhang@bham.ac.uk

Keywords: orbital angular momentum superposition, metasurface, multichannel

Superposition of orbital angular momentum (OAM) states has attracted considerable attention due to its application in diverse scientific areas, such as high-capacity optical communication, kinematic sensing, spin object detection, quantum memory, and generation of rotational states in Bose-Einstein condensation. For practical applications of OAM states, a simple approach to generate OAM beams and manipulate OAM superpositions in multiple channels at will is highly desirable. Here, we propose and experimentally demonstrate a facile metasurface approach to realize polarization-controllable multichannel superpositions of OAM states at will. Multiple OAM beams in separate channels are generated by a single metasurface for an incident Gaussian beam with circular polarization. By manipulating the polarization state of the incident

light, arbitrary control of the superpositions of various OAM states in multiple channels is realized. This approach provides a fast and efficient way for the manipulation of OAM superposition and significantly simplifies the experiment setup, which is of great importance for the current efforts in the fields of quantum entanglement, metrology, and optical data storage.

1. Introduction

Light can carry spin angular momentum (SAM) and orbital angular momentum (OAM), which are manifested as circular polarization and azimuthal phase structure of light beam, respectively. Light possessing OAM (namely optical vortex) has a helical phase structure described by $\exp(i\ell\theta)$, where θ is the azimuthal angle, ℓ is the topological charge of optical vortex corresponding to an orbital angular momentum of $\ell\hbar$ per photon[1]. Recently, the OAM of light has attracted considerable attention due to its promising applications, including high-capacity optical communications[2], optical tweezers[3], quantum memories[4], orbital angular momentum microlaser[5], and metrology[6]. Specially, a superposition of OAM states is of importance in classical physics and quantum sciences[7]. For instance, equal-weighted linear combination of OAM modes ($|\ell|=1$) with opposite signs gives rise to a vector beam that has radially distributed polarization in the plane transverse to the beam propagation direction. This kind of beam has been applied in improved focusing[8] and high-speed kinematic sensing[9]. Superposition of high-order OAM modes can be used for ultra-sensitive angular measurement and spin object detection[6]. Multi-OAM-state can also be used to generate arbitrary superposition of atomic rotational states in a Bose-Einstein

condensate (BEC)[10]. In addition, OAM entangled light beams are prime candidates for fundamental characterizations of quantum entanglements[11], especially the spin-orbit hybrid entanglement[12].

Despite the diverse applications of OAM ranging from metrology to quantum entanglements, there are fundamental or technical challenges for current techniques to efficiently generate and manipulate multi-OAM-state of light. It is possible to generate optical OAM beams using cylindrical lenses, spiral phase plates, and holograms. However, all these devices are polarization independent, which cannot be adopted in the promising quantum photonic applications related to the spin-to-OAM conversion. Recently, q-plates, which are made of liquid crystal, have been developed and employed in many research fields such as transformation of quantum information[13], and polarization-controlled OAM beam generation[7, 14]. Nevertheless, q-plates are not only susceptible to chemical degradation and sensitive to temperature, but also suffer from poor spatial resolution and complicated operation. To realize various superpositions of OAM states, the interferometer[4, 7, 15] consisting of OAM generator, beam-splitters and mirrors, are usually employed in quantum experiments. However, such an approach significantly increases the complexity and volume of experimental systems. In addition, the aberrations introduced by this scheme and the misalignment of the optical elements greatly decrease the system performance. Consequently, a simple, efficient, and compact approach to achieve multichannel, artificially controlled generation and superposition of OAM states at higher resolution is desirable in the broad range of applications mentioned above.

Metasurfaces, the two-dimensional analog of conventional metamaterials, have drawn considerable attention in the scientific community due to their exotic electromagnetic properties and potential breakthroughs for light manipulation[16]. Metasurface has been widely adopted in many applications such as lensing[17], spin-hall effect[18], hologram[16], and invisibility[19]. Although metasurface based OAM generators[16, 20] have been experimentally demonstrated, continuously polarization-controlled OAM superpositions in multiple channels with a single metasurface have not been explored so far. In this paper, we propose and experimentally demonstrate an efficient approach to generate multiple OAM states and arbitrarily control their superpositions. OAM states with different topological charges are realized in four separate channels using a single plasmonic metasurface consisting of space-variant arrays of gold nanoantennas without any additional optical elements. By simply controlling the polarization state of the incident light, this approach is capable of artificially and continuously manipulating various OAM superpositions in multiple channels. The combination of multichannel OAM generation, polarization-controlled OAM superposition, subwavelength resolution, broad spectral band, and compactness renders this technology very attractive for diverse applications in both classical physics and quantum sciences.

2. Method for multichannel polarization-controlled superpositions of OAM modes

Figure 1a presents a schematic illustration of a single pixel of a plasmonic reflective-type metasurface[17, 21]. The plasmonic metasurface is composed of three layers, i.e., a

gold ground layer, a silicon dioxide (SiO_2) spacer layer, and a top layer of gold nanorods. All the nanorods have same geometry but different orientation angles ϕ. When a right-handed circularly polarized (RCP) light beam shines on this metasurface, part of the reflected light maintains the same circular polarization and acquires an abrupt phase change 2ϕ (known as Pancharatnam-Berry phase). Thus, metasurfaces provide an efficient way to modify the phase of light in a space-variant manner. For the case of left-handed circularly polarized (LCP) incident light, the sign of the abrupt phase change is reversed (-2ϕ) [16, 21]. To generate off-axis multiple OAM states, the phase distribution is described as[22]

$$\Phi(x, y) = \arg(\sum_{j=1}^{N} E_j \exp(i(\ell_j \theta + \Delta\varphi_{j,x} + \Delta\varphi_{j,y}))) \quad (1)$$

where N is the total number of OAM states, E_j is the amplitude component of OAM state ℓ_j, θ is the azimuthal angle. $\Delta\varphi_{j,x}$ and $\Delta\varphi_{j,y}$ are respectively phase differences between neighboring pixels to generate phase gradients along x and y directions, which introduce the off-axis deflection for the OAM mode of interest[16, 23]. It is noted that the phase profile $\Phi(x, y)$ is not dependent on the wavelength, indicating that it can operate in the broadband.

The fabricated metasurfaces are subsequently employed for off-axis multi-OAM generation upon the illumination of the RCP incident light. One of the designed metasurfaces is schematically shown in **Figure 1**b, where four OAM beams with different topological charges ranging from $\ell = 1$ to $\ell = 4$ are generated when a RCP Gaussian beam impinges on it. To realize polarization-controlled superposition of

OAM states, one can design a phase profile that, upon the illumination of RCP light, can simultaneously generate a pair of off-axis OAM beams of basis ℓ_1 and ℓ_2 centrosymmetric with respect to the normal axis, as illustrated by **Figure 1**c. By switching the helicity of incident light from RCP to LCP, the propagating directions of two generated OAM beams are swapped with respect to the axis of incident light. Meanwhile, the signs of two topological charges are flipped, since the sign of the abrupt phase change introduced by the metasurface is dependent on the helicity of circular polarization[16] (see **Figure 1**c (ii)). An arbitrary polarized light beam can be decomposed into the superposition of two circularly polarized beams with opposite helicity (see **Figure 1**c (iii)), which can be described as

$$\Psi = A \cdot e^{i\vartheta} \left| R \right\rangle + B \cdot e^{-i\vartheta} \left| L \right\rangle \tag{2}$$

where A and B denote the amplitude coefficients of RCP and LCP light, ϑ represents the relative phase difference between the two orthogonal polarization states. Two kinds of superpositions of two OAM eigenstates with different circular polarizations are realized in two channels, which are $(A \cdot e^{i\vartheta} \left| R, \quad \ell_2 \right\rangle + B \cdot e^{-i\vartheta} \left| L, \quad -\ell_1 \right\rangle)$ and $(A \cdot e^{i\vartheta} \left| R, \quad \ell_1 \right\rangle + B \cdot e^{-i\vartheta} \left| L, \quad -\ell_2 \right\rangle)$ (see **Figure 1**c (iii) and (iv)). From the description of resultant beam, one can see that the superpositions of eigenstates in two channels are exactly dependent on the polarization state of incident light. Consequently, multichannel, arbitrary superposition of OAM states can be realized using a single reflective-type metasurface with the predesigned phase distribution.

To elucidate the mechanism of OAM superposition, the concept of Higher-order Poincaré sphere is introduced[24]. In analogy to the well-known Poincaré sphere for polarization state description, the Higher-order Poincaré sphere provides a framework for describing the total optical angular momentum including both the spin and orbital angular momentum. The two poles of the sphere represent the two eigenstates with different spin and angular momentum $|R,\ \ell_1\rangle$ and $|L,\ \ell_2\rangle$ corresponding to two Laguerre-Gauss (LG) transverse modes with opposite circular polarization states, respectively. It should be mentioned that both the values and signs of OAM eigenstates ℓ_1 and ℓ_2 can be different[25]. The superposition of LG modes with orthogonal circular polarization states can produce Poincaré beams, which have a spatial mode that correlates transverse spatial coordinates with states of polarization[26]. The detailed information is provided in the Supplementary section 1. **Figure 1**c (iv) shows the transformation between the easily manipulated polarization states represented on the fundamental Poincaré sphere and the higher-order states including both spin and angular momentum as depicted by Higher-order Poincaré sphere with circularly polarized OAM eigenstates ℓ_1 and ℓ_2, by means of a metasurface. The generation of required OAM eigenstates and their superposition process occur on the same metasurface by controlling the polarization state of the incident light.

3. Experimental results

To verify our proposed approach, we design and fabricate two samples for generating multiple OAM states and manipulating the superpositions of different OAM states in multiple channels. The fabrication process and experiment setup are given in Methods.

Figure 2 shows the first metasurface (META1) that generates the superposition of OAM states with topological charges of same absolute values but opposite signs in four output channels. Under the illumination of RCP light, two pairs of off-axis OAM beams are generated, i.e., $\left|R,\quad \ell_i\right\rangle$ (denoted by black dots along the horizontal direction) and $\left|R,\quad \ell_j\right\rangle$ (yellow dots along the vertical direction), respectively (see **Figure 2**a (i)). Here ℓ_i, ℓ_j are the topological charges. By changing the helicity of the incident light from RCP to LCP, the signs of all the topological charges of output OAM states are flipped (see **Figure 2**a (ii)), and the positions of the beams are changed to the corresponding centrosymmetric positions with respect to the center, accordingly. A linearly polarized (LP) incident light can be decomposed into two equal-weighted RCP and LCP components with a phase difference, the states of the output beams generated by the metasurface are $e^{i\vartheta}\left|R,\quad \ell_i\right\rangle + e^{-i\vartheta}\left|L,\quad -\ell_i\right\rangle$ and $e^{i\vartheta}\left|R,\quad \ell_j\right\rangle + e^{-i\vartheta}\left|L,\quad -\ell_j\right\rangle$, respectively. Specifically, two superpositions, i.e., OAM states with $\ell = 1$ and $\ell = -1$, and OAM states with $\ell = 3$ and $\ell = -3$, are generated. The scanning electron microscope (SEM) image of META1 is shown in **Figure 2**b. META1 is first characterized using LP light, whose polarization angles are set as 0 and $\pi/4$ (denoted by the red arrows), respectively. We measure the diffracted beams by recording the intensity profiles at the wavelength of 650 nm. For the case of LP incident light, a superposition of OAM modes with equal weight and opposite topological charges is easily realized. Moreover, the two OAM modes have opposite circular polarization. The superimposed mode can be diagnosed by passing through a linear polarizer forming an angle χ with respect to the horizontal axis (x axis) and the Jones matrix of the polarizer has the form

$$\begin{bmatrix} \cos^2\chi & \sin\chi\cos\chi \\ \sin\chi\cos\chi & \sin^2\chi \end{bmatrix} \quad (3)$$

The transmitted intensity profile can be expressed by

$$\mathrm{E} = \frac{1}{2}\left[1+\cos^2\left(\ell\theta+\vartheta+\chi\right)\right] \quad (4)$$

The transmitted intensity finds its minima at the azimuth angle $\theta_n = \frac{(2n-1)\pi}{2\ell} - \frac{\vartheta}{\ell} - \frac{\chi}{\ell}$ and has 2ℓ lobes, where $n = 1, 2, ...2\ell$. A good agreement between the simulated and measured results is achieved (**Figure 2**b). It should be noted that the combination of $|R, \quad \ell = 1\rangle$ and $|L, \quad \ell = -1\rangle$ with equal power can generate a radially polarized vector beam, which has been found in many applications due to its unique properties[7, 8, 27]. Since each OAM beam has a space-dependent profile of phase and amplitude in the plane perpendicular to its propagation direction, a coaxial superposition of two vortex beams with certain topological charges and orthogonal circular polarizations can generate a beam with a space-dependent polarization profile. The linear polarizer placed in a specific channel allows the two beams to interfere, producing an interferogram that determines the number of the lobes. Detailed explanation is given in the supplementary Section 5.

To characterize the functionality of polarization-controlled OAM superposition, the intensity profiles of output beams from META1 are measured at different polarization states of the incident light. A setup consisting of a Glan polarizer (GP), a half-wave plate (HP), and a quarter-wave plate (QP) is used to generate the required polarization states. Initially, five polarization states of the incident light, including right-handed

circular polarization, right-handed elliptical polarization, horizontal linear polarization, left-handed elliptical polarization, and left-handed circular polarization are chosen. The polarization states are geometrically represented by the points located along a meridian trajectory on the Poincaré sphere shown in **Figure 3**a. **Figure 3**a also shows the simulated and measured intensity profiles of diffracted beams at the wavelength of 650 nm with horizontal linear polarizer in front of the CCD camera. To further characterize the capability of arbitrary controlled superposition, another five polarization states located along the second meridian trajectory on the Poincaré sphere shown in **Figure 3**b are chosen, where the two circular eigenstates have a phase difference of $\pi/2$. Unsurprisingly, the introduced phase difference of $\pi/2$ between the eigenstates on the corresponding Higher-order Poincaré spheres results in the rotation of the intensity profiles, which is theoretically predicted and experimentally verified (see **Figure 3**b).

To evaluate the performance of this approach, we measure the power of each channel and calculate the conversion efficiency. The designed metasurface is characterized at a wavelength range of 640 – 940 nm. The relative powers in all the channels are nearly the same over a broad wavelength range (640 nm-880 nm), agreeing well with the theoretical design. The total conversion efficiency is defined by the total power of the output light from the four channels divided by the power of incident light. The conversion efficiency of META1 at wavelength of 650 nm is 12%. The maximum conversion efficiency is 50% at the wavelength of 820 nm. The experimental results are given in the Supplementary section 2.

To demonstrate the versatility and high performance of this platform, a second metasurface (META2) that can realize different hybrid superpositions of OAM states in four separate channels (**Figure 4**) is also developed. Four OAM beams with different topological charges ranging from $\ell = 1$ to $\ell = 4$ in separate channels are observed for an incident Gaussian beam with right-handed circular polarization (see **Figure 4**a (ii) and (iii)). An OAM beam with a topological charge of ℓ has a 'doughnut' intensity profile with a dark area in the beam centre. The radius of 'doughnut' , defined by the distance from the centre to the maximum intensity points is expressed by $r = w\sqrt{\ell / 2}$, where w is the beam radius[28]. By controlling the polarization of the incident beam, four cases of superpositions of OAM states in four separate output channels are realized. The four superpositions include $(\cos\theta \cdot e^{i\vartheta}|R,\ \ell = 1\rangle + \sin\theta \cdot e^{-i\vartheta}|L,\ \ell = -3\rangle)$, $(\cos\theta \cdot e^{i\vartheta}|R,\ \ell = 2\rangle + \sin\theta \cdot e^{-i\vartheta}|L,\ \ell = -4\rangle)$, $(\cos\theta \cdot e^{i\vartheta}|R,\ \ell = 3\rangle + \sin\theta \cdot e^{-i\vartheta}|L,\ \ell = -1\rangle)$, and $(\cos\theta \cdot e^{i\vartheta}|R,\ \ell = 4\rangle + \sin\theta \cdot e^{-i\vartheta}|L,\ \ell = -2\rangle)$, where θ determines the ratio of the amplitudes of the two component OAM beams. Each OAM superposition can be represented by a point on a Hybrid-order Poincaré sphere[25]. A similar method as above is used to characterize this metasurface. Although there are four different superpositions in all the channels, only the simulated and measured results of OAM superpositions $(\cos\theta \cdot e^{i\vartheta}|R,\ \ell = 1\rangle + \sin\theta \cdot e^{-i\vartheta}|L,\ \ell = -3\rangle)$ are given (see **Figure 4**b) here. By continuously changing the polarization state of incident light from RCP to LCP, the diameter of dark hole in the center of the generated intensity profile increases (see **Figure 4**b top), indicating the superposition of two OAM states evolves from the OAM state with $\ell_1 = 1$ to that with $\ell_3 = -3$. For elliptically polarized incident light, the

resultant beam is the superposition of two OAM states with different components, which is further verified by the transmitted intensity profiles through a horizontal linear polarizer (see **Figure 4**b bottom). Actually, the output beam becomes composite-vortex beam which contains a vortex of charge $\ell_1 = 1$ in the centre of the beam surrounded by $|\ell_1 - \ell_3| = 4$ singly charged peripheral vortices with the same sign of ℓ_3 located at the same radial distance (see Supplementary section 1). The experimental results on the superposition of $(e^{i\vartheta}|R,\ \ell = 2\rangle + e^{-i\vartheta}|L,\ \ell = -4\rangle)$ are available in the Supplementary **Figure S2**. It should be mentioned that the rotation of intensity profile $\Delta\Gamma_G$ due to the ℓ-dependent Gouy phase is theoretically predicted[28] and experimentally observed (see **Figure 4**). Therefore, this approach provides a simple way to measure the Gouy phase. The detailed explanation about Gouy rotation and the polarization profile of the resultant beams with hybrid superposition are given in the Supplementary section 4 and section 5, respectively.

4. Conclusion

The metasurfaces presented in our work feature the combination of a number of important functionalities and advantages such as multichannel OAM generation, polarization-controlled OAM superposition, subwavelength resolution, broadband, and compactness, which have a broad impact in the areas of photonics, quantum sciences, and fundamental physics. Superposition of optical beams with opposite circular polarizations and orbital angular momenta can be used to create a light beam with non-trivial polarization and phase properties. A linear combination of equal-weighted RCP optical vortex beam with topological charge $\ell = 1$ and LCP optical vortex beam with

topological charge $\ell = -1$ can generate a radial vector beam, which has been applied in high resolution lithography[7], quantum memory[4], and metrology[8]. Complex superposition of light beams with opposite circular polarizations and different orbital angular momentum states (See supplementary Section 5) may lead to interesting polarization topologies such as polarization singularities[29] and polarization Möbius strips[30]. The preparation of these structured light modes like Möbius strips may be important for complex light beam engineering. Our approach possesses several practical and technical advantages over conventional ways for producing OAM superposition, such as Segnac interferometer consisting of OAM beam generator, beam-splitters, Dove prism, and mirrors[7]. First, our work overcomes the various hurdles such as misalignment, phase aberration, and complex experimental setup. Without any additional optical elements, the superposition of OAM modes with arbitrary amplitude and phase ratios in multichannels can be easily realized by manipulating the polarization state of the input light. Furthermore, this approach provides a unique tool for investigating the entanglement between polarization and orbital angular momentum of photons. Due to its intrinsic multichannel nature, the proposed approach can be readily extended to higher dimensional[31] and multi-particle entanglement[32]. Our proposed approach is very robust since it can be applied not only to reflective-type metasurfaces that can operate in broadband with high efficiency, but also to transmissive metasurfaces that can generate geometric phase, including silicon nanofins[33] or titanium dioxide nanofins[34]. The capability to generate four individual OAM beams and arbitrarily manipulate OAM superposition using a single metasurface

with a minimal footprint, paves the way for highly compact meta-devices in quantum experimental systems[35].

In conclusion, we propose and experimentally demonstrate a novel approach to realize OAM superpositions in multiple channels using a single plasmonic metasurface. Arbitrary manipulation of OAM superpositions in four channels is observed by controlling the polarization state of the incident light. Our work solves several major issues associated with OAM research: multichannel OAM generation, polarization-controllable OAM superposition, higher resolution, broadband, and compactness, rendering this technology very attractive for diverse applications such as photonics, quantum science, and fundamental physics. Due to the simplicity and robustness of our design, we believe this work to be of fundamental significance and useful for the practical application of OAM devices.

5. Experimental Section

Sample fabrication. To fabricate the designed metasurface, the standard electron-beam lithography (EBL) and lift-off process are used. Firstly, the gold background layer (150nm) and the SiO_2 spacer (85 nm) are deposited onto a silicon substrate by using an electron beam evaporator. Then, the positive poly methyl methacrylate (PMMA) resist film is spin coated on the SiO_2 spacer layer and baked at 180℃ for five minutes. Then, the nanostructures are defined on the PMMA film by EBL (Raith PIONEER). Prior to gold deposition, a titanium layer of ~3 nm is deposited on the silicon dioxide (SiO_2) layer for adhesion purpose. After that, a 30 nm gold film is deposited on the sample via

electron beam evaporation. Finally, the metasurface structure is achieved by a subsequent lift-off procedure.

Experimental setup. The metasurface samples are mounted on a three-dimensional translation stage and exposed to the light from a tunable supercontinuum laser source (NKT-SuperK EXTREME) which covers the wavelength range from 640 nm to 1100 nm. A setup consisting of a Glan polarizer (GP), a half-wave plate (HP), and a quarter-wave plate (QP) is used to generate the required polarization states. Then the collimated Gaussian beam impinges upon metasurface at normal incidence with a weak focus by a lens with a focal length of 100 mm. The measured intensity patterns of reflected output beam are captured using a color CCD camera. The off-axis design not only simplifies the experimental characterization, but also facilitates the practical applications.

Supporting Information

Supporting Information is available online from the Wiley Online Library or from the author.

Acknowledgements

This work is supported by the Engineering and Physical Sciences Research Council of the United Kingdom (Grant Ref: EP/M003175/1) .

Received: ((will be filled in by the editorial staff))
Revised: ((will be filled in by the editorial staff))
Published online: ((will be filled in by the editorial staff))

References

[1] L. Allen, M. W. Beijersbergen, R. J. C. Spreeuw, J. P. Woerdman, *Phys. Rev. A* **1992**, *45*, 8185.

[2] a) A. E. Willner, H. Huang, Y. Yan, Y. Ren, N. Ahmed, G. Xie, C. Bao, L. Li, Y. Cao, Z. Zhao, *Advances in Optics and Photonics* **2015**, *7*, 66; b) J. Wang, J.-Y. Yang, I. M. Fazal, N. Ahmed, Y. Yan, H. Huang, Y. Ren, Y. Yue, S. Dolinar, M. Tur, *Nat. Photonics* **2012**, *6*, 488.

[3] M. Padgett, R. Bowman, *Nat. Photonics* **2011**, *5*, 343.

[4] A. Nicolas, L. Veissier, L. Giner, E. Giacobino, D. Maxein, J. Laurat, *Nat. Photonics* **2014**, *8*, 234.

[5] P. Miao, Z. Zhang, J. Sun, W. Walasik, S. Longhi, N. Litchinitser, L. Feng, *Science*, **2016**, *353*, 464.

[6] a) M. P. Lavery, F. C. Speirits, S. M. Barnett, M. J. Padgett, *Science* **2013**, *341*, 537; b) V. D'Ambrosio, N. Spagnolo, L. Del Re, S. Slussarenko, Y. Li, L. C. Kwek, L. Marrucci, S. P. Walborn, L. Aolita, F. Sciarrino, *Nat. Commun.* **2013**, *4*, 2432.

[7] a) A. Vaziri, G. Weihs, A. Zeilinger, J. Opt. B: Quantum Semiclassical Opt. **2002**, *4*, S47; b) L. Marrucci, E. Karimi, S. Slussarenko, B. Piccirillo, E. Santamato, E. Nagali, F. Sciarrino, J. Opt. **2011**, *13*, 064001.

[8] R. Dorn, S. Quabis, G. Leuchs, *Phys. Rev. Lett.* **2003**, *91*, 233901.

[9] S. Berg-Johansen, F. Töppel, B. Stiller, P. Banzer, M. Ornigotti, E. Giacobino, G.

Leuchs, A. Aiello, C. Marquardt, *Optica* **2015**, *2*, 864.

[10]a) M. Andersen, C. Ryu, P. Cladé, V. Natarajan, A. Vaziri, K. Helmerson, W. Phillips, *Phys. Rev. Lett*. **2006**, *97*, 170406; b) K. Sun, C. Qu, C. Zhang, *Phys. Rev. A* **2015**, *91*, 063627.

[11] A. Mair, A. Vaziri, G. Weihs, A. Zeilinger, *Nature* **2001**, *412*, 313.

[12] a) E. Karimi, J. Leach, S. Slussarenko, B. Piccirillo, L. Marrucci, L. Chen, W. She, S. Franke-Arnold, M. J. Padgett, E. Santamato, *Phys. Rev. A* **2010**, *82*, 022115; b) R. Fickler, *Quantum Entanglement of Complex Structures of Photons*, Springer, **2015**; c) D. Bhatti, J. von Zanthier, G. S. Agarwal, *Phys. Rev. A* **2015**, *91*, 062303.

[13] E. Nagali, F. Sciarrino, F. De Martini, L. Marrucci, B. Piccirillo, E. Karimi, E. Santamato, *Phys. Rev. Lett.* **2009**, *103*, 013601.

[14] a) E. Karimi, S. Slussarenko, B. Piccirillo, L. Marrucci, E. Santamato, *Phys. Rev. A* **2010**, *81*, 053813; b) D. Naidoo, F. S. Roux, A. Dudley, I. Litvin, B. Piccirillo, L. Marrucci, A. Forbes, *Nat. Photonics* **2016**, *10*, 327.

[15] R. Fickler, M. Krenn, R. Lapkiewicz, S. Ramelow, A. Zeilinger, *Sci. Rep*. **2013**, *3*, 1914.

[16] a) N. F. Yu, P. Genevet, M. A. Kats, F. Aieta, J. P. Tetienne, F. Capasso, Z. Gaburro, *Science* **2011**, *334*, 333. b) L. Huang, X. Chen, H. Mühlenbernd, G. Li, B. Bai, Q. Tan, G. Jin, T. Zentgraf, S. Zhang, *Nano Lett.* **2012**, *12*, 5750; c) A. Arbabi, Y. Horie, M. Bagheri, A. Faraon, *Nat. Nanotechnol*. **2015**, *10*, 937; d) M. Q. Mehmood, S. Mei, S. Hussain, K. Huang, S. Y. Siew, L. Zhang, T. Zhang, X. Ling, H. Liu, J. Teng, A. Danner, S. Zhang, C. W. Qiu, *Adv. Mater.* **2016**, *28*, 2533; e) D. Lin, P. Fan,

E. Hasman, M. L. Brongersma, *Science* **2014**, *345*, 298; f) H. Cheng, Z. Liu, S. Chen, J. Tian, *Adv. Mater.* **2015**, *27*, 5410.

[17] G. X. Zheng, H. Muhlenbernd, M. Kenney, G. X. Li, T. Zentgraf, S. Zhang, *Nat. Nanotechnol.* **2015**, *10*, 308.

[18] X. Yin, Z. Ye, J. Rho, Y. Wang, X. Zhang, *Science* **2013**, *339*, 1405.

[19] X. Ni, Z. J. Wong, M. Mrejen, Y. Wang, X. Zhang, *Science* **2015**, *349*, 1310.

[20] E. Maguid, I. Yulevich, D. Veksler, V. Kleiner, M. L. Brongersma, E. Hasman, *Science* **2016**, aaf3417.

[21]D. Wen, F. Yue, G. Li, G. Zheng, K. Chan, S. Chen, M. Chen, K. F. Li, P. W. Wong, K. W. Cheah, E. Yue Bun Pun, S. Zhang, X. Chen, *Nat. Commun.* **2015**, *6*, 8241.

[22] S. Li, C. Li, J. Liu, L. Zhu, Z. Xu, J. Zhou, Q. Yang, J. Wang, *2014 The European Conference on Optical Communication (ECOC)*. **2014**.

[23] a) D. Wen, F. Yue, S. Kumar, Y. Ma, M. Chen, X. Ren, P. E. Kremer, B. D. Gerardot, M. R. Taghizadeh, G. S. Buller, *Opt. Express* **2015**, *23*, 10272; b) S. Chen, Y. Cai, G. Li, S. Zhang, K. W. Cheah, *Laser Photonics Rev.* **2016**, *10*, 322.

[24] a) G. Milione, H. I. Sztul, D. A. Nolan, R. R. Alfano, *Phys. Rev. Lett.* **2011**, *107*, 053601; b) G. Milione, S. Evans, D. Nolan, R. Alfano, *Phys. Rev. Lett.* **2012**, *108*, 190401.

[25] X. Yi, Y. Liu, X. Ling, X. Zhou, Y. Ke, H. Luo, S. Wen, D. Fan, *Phys. Rev. A* **2015**, *91*, 023801.

[26] E. J. Galvez, S. Khadka, W. H. Schubert, S. Nomoto, *Appl. Opt.* **2012**, *51*, 2925.

[27] V. D'Ambrosio, E. Nagali, S. P. Walborn, L. Aolita, S. Slussarenko, L. Marrucci, F. Sciarrino, *Nat. Commun.* **2012**, *3*, 961.

[28] S. Baumann, D. Kalb, L. MacMillan, E. Galvez, *Opt. Express* **2009**, *17*, 9818.

[29] F. Cardano, E. Karimi, L. Marrucci, C. de Lisio, E. Santamato, *Opt. Express* **2013**, *21*, 8815.

[30] T. Bauer, P. Banzer, E. Karimi, S. Orlov, A. Rubano, L. Marrucci, E. Santamato, R. W. Boyd, G. Leuchs, *Science* **2015**, *347*, 964.

[31] M. Malik, M. Erhard, M. Huber, M. Krenn, R. Fickler, A. Zeilinger, *Nat. Photonics* **2016**, *10*, 248.

[32] a) B. Jack, A. M. Yao, J. Leach, J. Romero, S. Franke-Arnold, D. G. Ireland, S. M. Barnett, M. J. Padgett, *Phys. Rev. A* **2010**, *81*, 043844; b) B. Hiesmayr, M. de Dood, W. Löffler, *Phys. Rev. Lett.* **2016**, *116*, 073601.

[33] S. Kruk, B. Hopkins, I. I. Kravchenko, A. Miroshnichenko, D. N. Neshev, Y. S. Kivshar, *APL Photonics*, **2016**, *1*, 030801.

[34] M. Khorasaninejad, W. Chen, R. C. Devlin, J. Oh, A. Y. Zhu, F. Capasso, *Science* **2016**, *352*, 1190.

[35] T. Lei, M. Zhang, Y. Li, P. Jia, G. N. Liu, X. Xu, Z. Li, C. Min, J. Lin, C. Yu, H. Niu, X. Yuan, *Light Sci. Appl.* **2015**, *4*, e257.

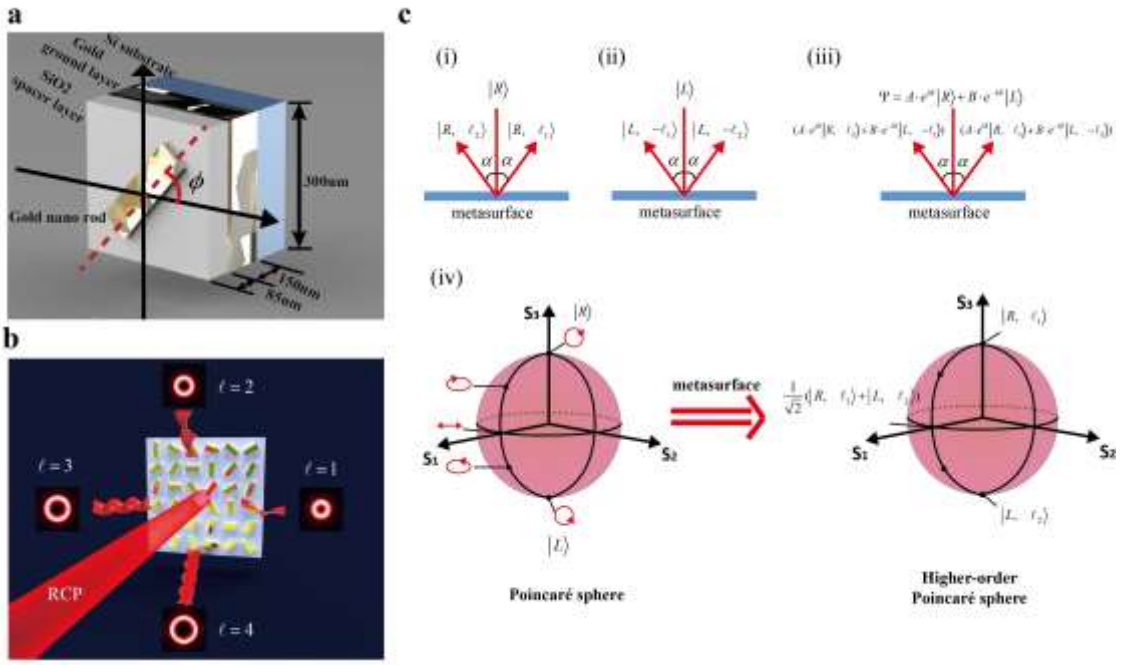

Figure 1. Schematic illustration of multichannel polarization-controllable superposition of OAM states via a single plasmonic metasurface. a, A single pixel of reflective-type metasurface. The metasurface is composed of three layers, i.e., a top layer of gold nanorods array (30 nm), a silicon dioxide (SiO_2) spacer layer (85 nm) and a gold ground layer (150 nm) sitting on a silicon substrate. The size of each pixel is 300 nm × 300 nm. Each nanorod is 220 nm long and 80 nm wide. b, Schematic of off-axis multi-OAM generation. Four OAM states with topological charges ranging from $\ell = 1$ to $\ell = 4$ are generated under illumination of RCP light. Considering the practical application, the off-axis design is employed in this approach. By changing the helicity of incident light from RCP to LCP, the positions of all the OAM beams are changed to their centrosymmetric positions with respect to the axis of incident light. Meanwhile, the signs of all the topological charges are changed from plus to minus. c, Schematics of polarization-controlled superposition of OAM states. The polarization states of the incident light in (i), (ii) and (iii) are RCP, LCP, and arbitrary polarization state, respectively. Upon the illumination of an incident beam with an arbitrary polarization state, the resultant beam is the superposition of RCP and LCP OAM beams with different components (*A* for RCP and *B* for LCP) and a phase difference $e^{i\vartheta}$. (iv) Illustration of the superposition process with the aid of two types of Poincaré spheres. The polarization state of the incident light is represented by a point on the fundamental Poincaré sphere, while the superposition of OAM eigenstates ℓ_1 and ℓ_2 is represented by a higher-order Poincaré sphere. A metasurface bridges the gap between the two different types of Poincaré spheres.

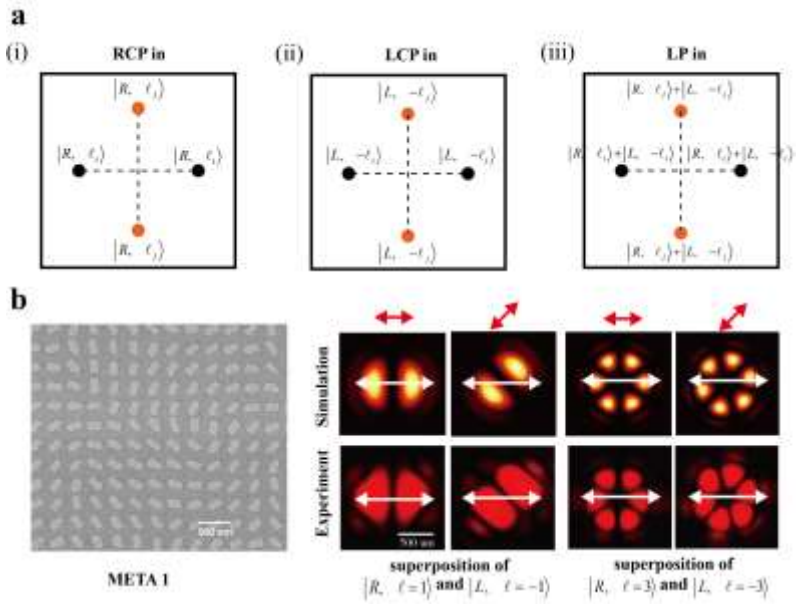

Figure 2. Schematic of the four-channel OAM superpositions, SEM image of metasurface, and numerically calculated and experimentally observed superpositions of OAM states. a, The generation of two kinds of OAM modes and their superpositions in four channels. (i) Upon the illumination of RCP input light, two pairs of off-axis OAM beams are generated, i.e., $|R,\ \ell_i\rangle$ (denoted by black dots) and $|R,\ \ell_j\rangle$ (denoted by yellow dots), respectively. (ii) The positions of OAM states and their signs are changed for LCP input light. (iii) Equal-weighted OAM states superpositions occur under the illumination of linearly polarized (LP) input light. b, SEM image and numerically calculated and experimentally observed superpositions of OAM states. This metasurface produces two kinds of superpositions, one for OAM states with $\ell = 1$ and $\ell = -1$, and another one for OAM states with $\ell = 3$ and $\ell = -3$. The polarization angle of incident linearly polarized light and the direction of the polarizer's transmission axis in front of the CCD camera are respectively denoted by the red double-headed arrows and the white double-headed arrows.

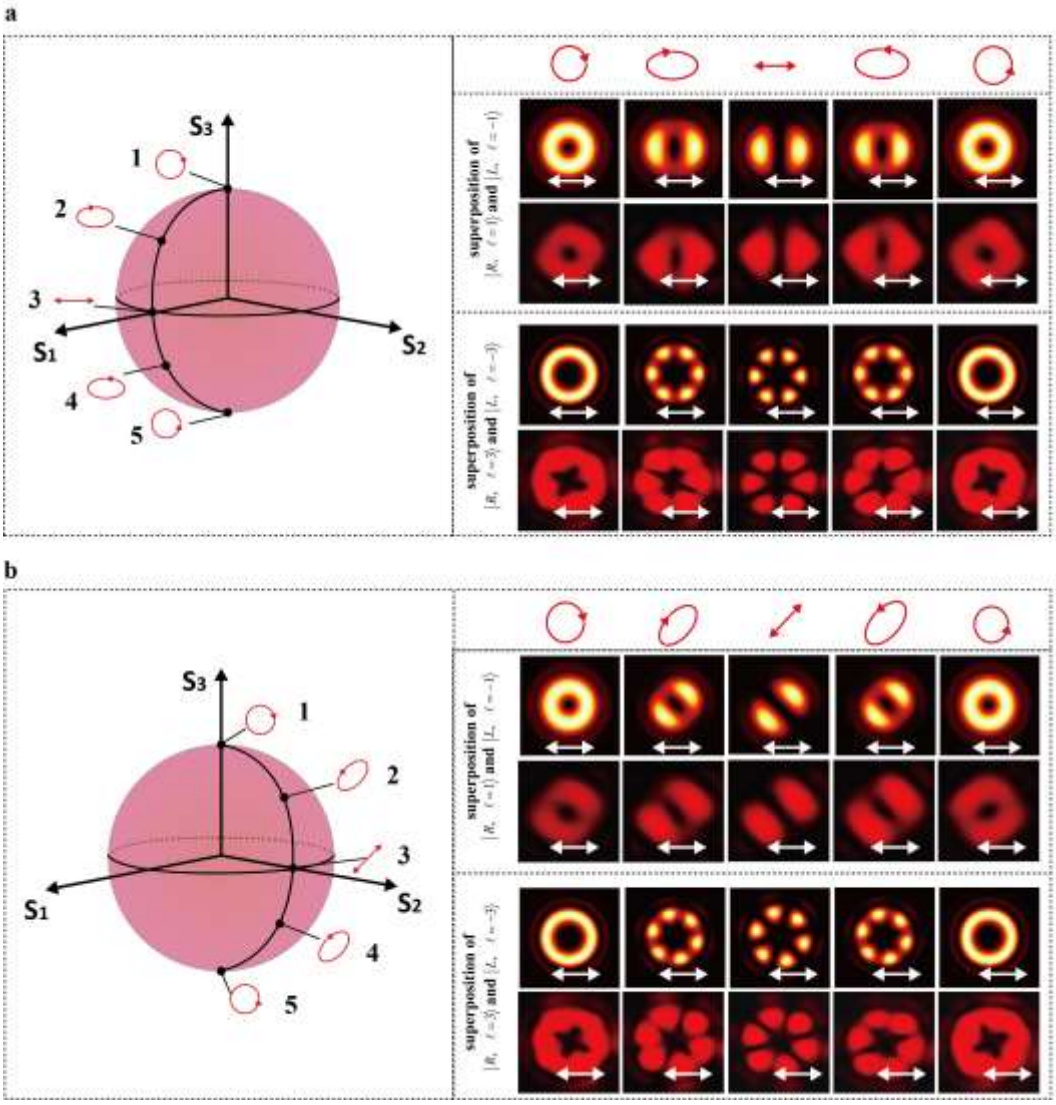

Figure 3. Simulated and experimental results of polarization-controllable superposition of OAM states with the metasurface shown in Figure 2b. a and b, Simulated and measured intensity profiles of generated beams corresponding to superpositions of OAM eigenstates. Several polarization states are chosen along two different meridian trajectories on the Poincaré sphere. The red symbols on the Poincaré sphere represent the polarization states of incident light. The direction of the analyzing polarizer's axis is denoted by the white double-headed arrows.

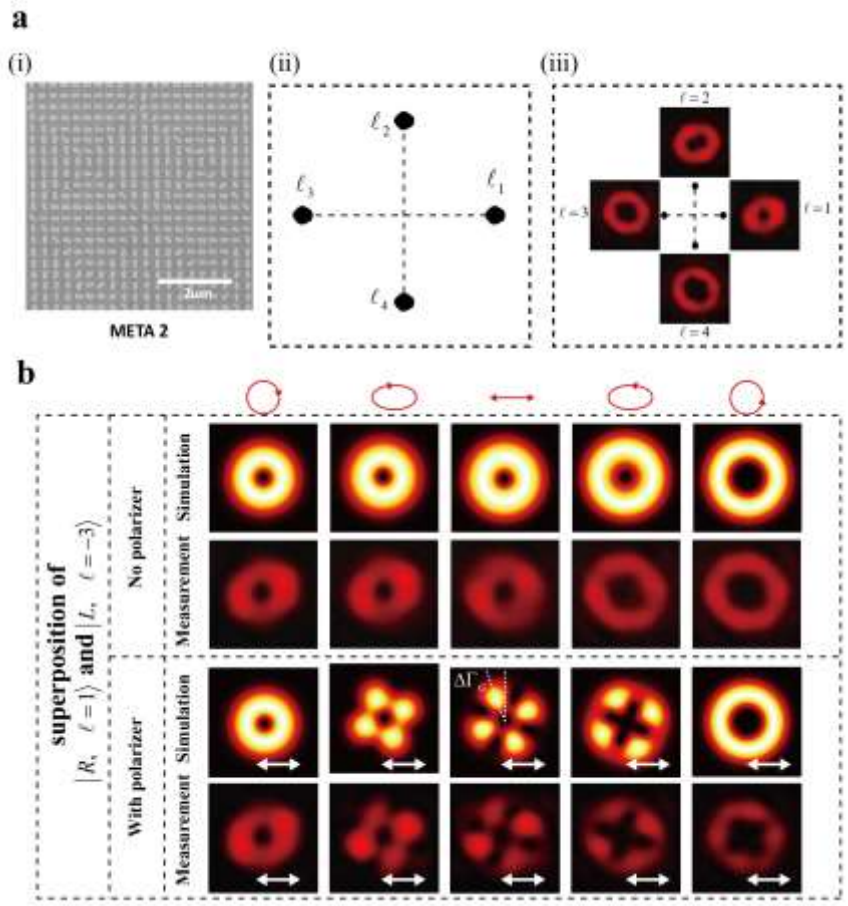

Figure 4. Metasurface for realization of the four-channel OAM hybrid superpositions and part of the experimental results. a, (i) SEM image of the fabricated metasurface. (ii) Upon the illumination of RCP input light, four OAM beams with different topological charges ℓ_i ($i=1,2,3,4$) are generated. (iii) Measured intensity profiles of four OAM beams generated under the illumination of an RCP Gaussian beam. b, Simulated and experimentally measured intensity profiles of the hybrid superpositions of OAM modes $|R,\ \ell=1\rangle$ and $|L,\ \ell=-3\rangle$. The OAM superposition of $|R,\ \ell=2\rangle$ and $|L,\ \ell=-4\rangle$ is given in the Supplementary Figure S2. $\Delta\Gamma_G$ is the Gouy rotation introduced by the Gouy phase difference between the component beams during propagation.

Submitted to ADVANCED MATERIALS

Supporting Information

for *Adv. Mater.*, DOI: 10.1002/adma.((please add manuscript number))

Supplementary of
Multichannel Polarization-Controllable Superpositions of Orbital Angular Momentum States

Fuyong Yue, Dandan Wen, Chunmei Zhang, Brian D. Gerardot, Wei Wang, Shuang Zhang, Xianzhong Chen**

Supplementary Section 1. Superposition of orbital angular momentum (OAM) modes with orthogonal circular polarizations.

The OAM states of light can be described mathematically as Laguerre-Gaussian (LG) modes, which are solutions of the paraxial Helmholtz equation in cylindrical coordinates. The LG mode is characterized by two indices p and ℓ [1], which refer to the radial nodes in its amplitude and azimuthal phase dependence, respectively. In this work, we consider the case of singly-ringed modes with $p = 0$. The field distribution of LG modes with a topological charge ℓ can be expressed as[1]

$$LG^{\ell}(r,\phi,z) = \left(\frac{2}{\pi\,|\,\ell\,|\,!}\right)^{1/2} \frac{1}{w(z)} \left(\frac{r\sqrt{2}}{w(z)}\right)^{|\ell|} e^{-r^2/(w(z))^2} e^{-i\ell\phi} e^{i(kz - kr^2/(2R(z)))} e^{i\varphi(\ell)} \qquad \text{(S1)}$$

where r, ϕ, z are the cylindrical coordinates, $w(z) = w_0\sqrt{2 + z^2 / z_R^2}$ is the beam radius at a propagation distance z, the constant w_0 is the beam waist, k is the wave number, $R(z) = (z_R^2 + z^2)/z$ denotes the radius of curvature of the wavefront, $\varphi(\ell) = (|\,\ell\,| + 1)\tan^{-1}(z / z_R)$ is the ℓ-dependent Gouy phase[2], and $z_R = kw_0^2 / 2$ is the Raleigh range. The LG mode has a 'doughnut' intensity profile due to the phase

singularity in the beam centre. The distance from the centre to points where the intensity is maximum is given by

$$\Omega = \sqrt{\frac{\ell}{2}} w(z) \tag{S2}$$

The superposition of LG modes with orthogonal circular polarizations produces Poincaré beams which have a spatial mode that correlates transverse spatial coordinates with states of polarization[3]. Any pure state of polarization can be represented with circular polarization bases as

$$\left|\Psi\right\rangle = \frac{1}{\sqrt{2}}(\cos\theta e^{i\vartheta}\left|R\right\rangle + \sin\theta e^{-i\vartheta}\left|L\right\rangle) \tag{S3}$$

where $\cos\theta$ and $\sin\theta$ are the amplitudes of two orthogonal circular components $\left|R\right\rangle$ and $\left|L\right\rangle$, respectively, ϑ refers to the phase difference between these two components. Under the illumination of a Gaussian beam ($LG^{\ell=0}$) with a polarization state described by Equation (S3) upon the metasurface, the resultant beam is the superposition of two LG modes with orthogonal circular polarizations. Consider the superposition of two LG modes with topological charges ℓ_1 and ℓ_2, the resultant beam can be expressed as

$$V = \frac{1}{\sqrt{2}}(\cos\theta \cdot LG^{\ell_1} \cdot e^{i\vartheta}\left|R,\quad \ell_1\right\rangle + \sin\theta \cdot LG^{\ell_2} \cdot e^{-i\vartheta}\left|L,\quad \ell_2\right\rangle) \tag{S4}$$

To clearly analyze the resultant beam, the results are divided into two cases: $\ell_1 = -\ell_2$ and $\ell_1 \neq -\ell_2$.

1. Case $\ell_1 = -\ell_2$

We can rewrite Equation (S4) with Jones vector as

$$V = \frac{G^{\ell}}{\sqrt{2}}(\cos\theta e^{i(\ell\phi+\vartheta)}\left|R\right\rangle + \sin\theta e^{-i(\ell\phi+\vartheta)}\left|L\right\rangle) \tag{S5}$$

where $\ell = \ell_1 = -\ell_2$, $G^{\ell} = \left(\frac{2}{\pi |\ell|!}\right)^{1/2} \frac{1}{w(z)} \left(\frac{r\sqrt{2}}{w(z)}\right)^{|\ell|} e^{-r^2/(w(z))^2} e^{i(kz - kr^2/(2R))} e^{i\varphi(\ell)}$. When $\theta = \frac{\pi}{4}$, the two circular components have equal intensities. The polarization state at every point of the beam's transverse plane is linear polarization with an orientation angle of $\ell\phi + \vartheta$. For $\ell = 1$, the vector beam is the well-studied radial vector beam for $\vartheta = 0$, and the azimuthal vector beam for $\vartheta = \frac{\pi}{2}$.

When θ is within the limit of (0, π/4) or (π/4, π/2), the polarization state at every point is elliptical polarization. The ellipticity is determined by θ, and the azimuthal angle is $\ell\phi + \vartheta$. The resultant beams are respectively right- and left-handed circularly polarized optical vortices for $\theta = 0$ and $\theta = \pi / 2$.

The Poincaré beams generated by the superposition of LG modes with orthogonal circular polarizations can be diagnosed by passing through a linear polarizer with orientation angle χ with respect to the horizontal axis. The transmitted intensity is proportional to $\cos^2(\ell\phi + \vartheta + \chi)$, and it has $2|\ell|$ minima at angles[3]

$$\phi_m = \frac{(2a-1)\pi}{2\ell} - \frac{\vartheta}{\ell} - \frac{\chi}{\ell} \tag{S6}$$

where $a = 1, 2, \ldots 2|\ell|$.

2. Case $\ell_1 \neq -\ell_2$

The Equation (S4) can be rewritten as

$$V = \frac{1}{\sqrt{2}} e^{i(\ell_1 + \ell_2)\phi/2} (e^{i\delta} \cos\theta \cos\beta |R\rangle + e^{-i\delta} \sin\theta \sin\beta |L\rangle) \tag{S7}$$

where

$$\beta = \tan^{-1}\left(\frac{G^{\ell_2}}{G^{\ell_1}}\right) \tag{S8}$$

$$\delta = \frac{(\ell_1 - \ell_2)\phi}{2} + \vartheta \tag{S9}$$

The polarization state at every point is determined by the three parameters θ, β, δ. If $|\ell_1| < |\ell_2|$, the polarization state evolves from right circularly polarized to left circularly polarized when moving the position from the centre to the edge of the beam. Interestingly, when $\ell_1 = 0$ and $\ell_2 = 1$, the resultant beam refers to full Poincaré beams, which have all states of polarization represented on a Poincaré sphere[4].

After the resultant beam passes through a linear polarizer, the output beam becomes composite-vortex beam which contains a vortex of charge ℓ_1 in the centre of the beam surrounded by $|\ell_1 - \ell_2|$ singly charged peripheral vortices with the same sign of ℓ_2 located at the same radial distance[2]

$$d = \frac{w(z)}{\sqrt{2}} \left(\frac{\ell_2!}{\ell_1!} (\tan\theta)^2 \right)^{\frac{1}{2(|\ell_2| - |\ell_1|)}} \tag{S10}$$

Supplementary Section 2. Conversion efficiency of metasurface.

To evaluate the performance of this approach and determine the conversion efficiency, we measured the power of each channel and calculated the relative power of each channel and the total conversion efficiency. **Figure S1** (a) shows the measured relative power of each channel where the total output power of four channels is normalized to unity. As can be seen from the measurement results each channel has one-quarter of the total output power over a broad wavelength range (640 nm-880 nm), which agrees well with the theoretical design. The total conversion efficiency is defined by the total power of the output light from the four channels divided by the power of incident light. By

measuring the total output powers and comparing these values with the power of input light, the dependence of conversion efficiency on the wavelength is given in **Figure S1** (b). The designed metasurface is characterized at a wavelength range of 640 – 940 nm, and the maximum conversion efficiency is 50% at the wavelength of 820 nm.

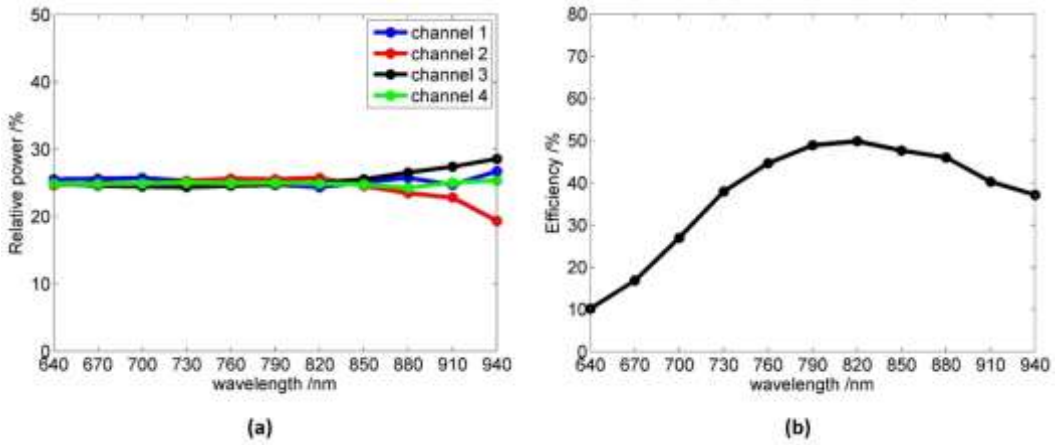

Figure S1. Relative power of each channel and total conversion efficiency. (a) Measured relative power in each channel of the metasurface. (b) Experimentally obtained conversion efficiency of the metasurface. The conversion efficiency is defined as the total power of four output beams divided by the power of incident light.

Supplementary Section 3. Experiment results of hybrid superposition of OAM modes.

In order to further explore the performance of this approach, we fabricate and characterize META 2 which is capable of achieving four different hybrid superpositions of OAM states in four separate channels. Under the illumination of an RCP Gaussian beam, four off-axis OAM beams with topological charges from $\ell = 1$ to $\ell = 4$ are generated simultaneously. To realize the off-axis reflection, the phase differences

between neighbouring pixels to generate phase gradients for OAM states with $|\ell|=1$ are $\Delta\varphi_x = \pi/5,\ \Delta\varphi_y = 0$, and those for OAM states with $|\ell|=3$ are $\Delta\varphi_x = 0,\ \Delta\varphi_y = \pi/5$. Arbitrary control of four hybrid superpositions of OAM states is realized by manipulating the polarization state of incident light. The polarization states of incident light are chosen to be, right-handed circular polarization, right-handed elliptical polarization, horizontal linear polarization, left-handed elliptical polarization, and left-handed circular polarization. **Figure S2** shows the simulated and measured results of hybrid-OAM superposition states $|R,\ \ \ell=2\rangle$ and $|L,\ \ \ell=-4\rangle$ with and without a linear polarizer in front of the CCD camera.

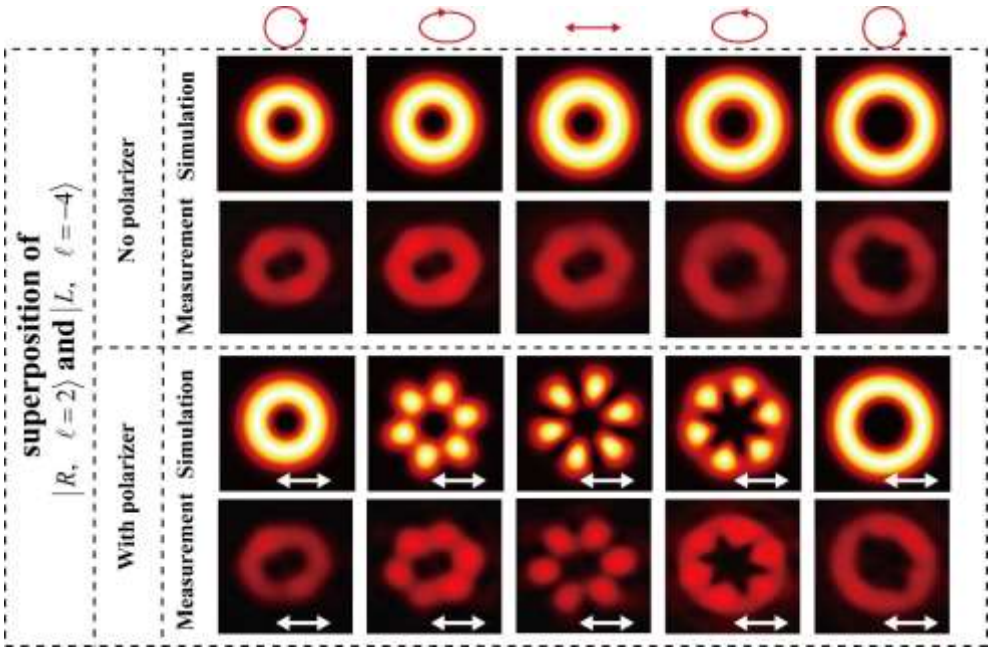

Figure S2. Simulated and measured intensity profiles of hybrid-OAM superposition states $|R,\ \ \ell=2\rangle$ and $|L,\ \ \ell=-4\rangle$. The polarization states of incident light and the direction of the polarizer's transmission axis in front of the CCD camera are respectively denoted by the red symbols and the white double-headed arrows.

Supplementary Section 4. Gouy rotation of the beam profile.

When the LG beam propagates along the optical path after focused, it acquires a ℓ-dependent Gouy phase[5] which is proportional to the fundamental Gouy phase $\tan^{-1}(z/z_R)$. It is given by

$$\Gamma_G = (2p+|\ell|+1)\tan^{-1}(z/z_R) \quad \text{(S11)}$$

Note that we consider the case where the radial index parameter of LG beam $p=0$, the field distribution of the beam is a single ring that contains a phase vortex of charge ℓ at its centre. When the composite beam formed by collinear superpositions of LG beams with topological charges of ℓ_1 and ℓ_2 propagates, the intensity profile rotates about the beam axis if $|\ell_1| \neq |\ell_2|$ since there is Gouy phase difference between the component beams. When $|\ell_1| = |\ell_2|$, there is no rotation. More details about the explanations can be found in Ref.[2].

Supplementary Section 5. Polarization distributions of the output beams.

A light beam with an arbitrary polarization state can be decomposed into two opposite circularly polarized beams with various components. Due to the space-dependent profile of phase and amplitude for an OAM beam in the plane perpendicular to its propagation direction, a coaxial superposition of two vortex beams with certain topological charges could generate a beam that has space-dependent polarization profile. For example, a cylindrical vector beam (radially or azimuthally polarized beams) can be realized by the superposition of two beams with different circular polarizations and topological charges of $\ell = 1$ and $\ell = -1$ (See Figure 2 in main text). The Full Poincaré

beam that possesses the polarization states within the beam cross section span the entire surface of the Poincaré sphere, can be constructed by a superposition of a Gaussian beam and a vortex beam with orthogonal circular polarizations. **Figure** S3 shows the polarization distributions of the output beam generated by META1 and META2. A linear polarizer placed in a specific channel allows the two beams to interfere, producing an interferogram that determines the number of the lobes. The transmission direction of the polarizer is set along the horizontal direction. It should be noted that the Gouy phase is not considered here. In fact, the evolution of the Gouy phase along propagation (see Section 4) will cause the rotation of the polarization pattern.

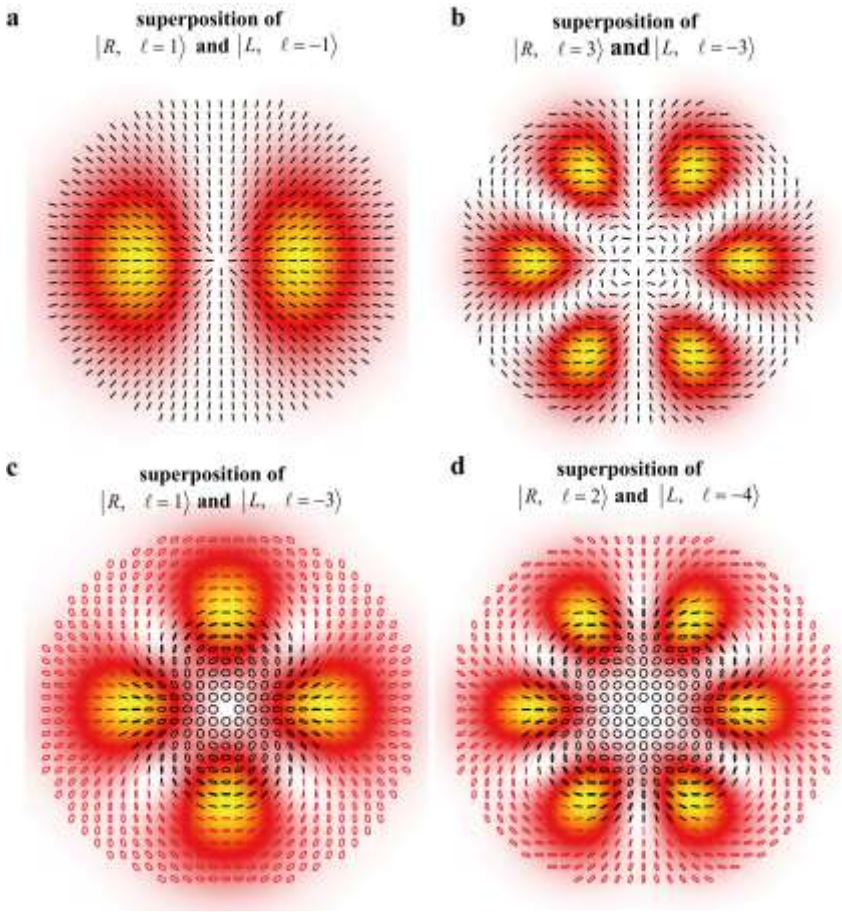

Figure S3. The simulated polarization profile at the cross section of output beam from META 1 and META 2. The superpositions of a. $|R,\ \ell=1\rangle$ and $|L,\ \ell=-1\rangle$, b.

$|R, \quad \ell = 3\rangle$ and $|L, \quad \ell = -3\rangle$, c. $|R, \quad \ell = 1\rangle$ and $|L, \quad \ell = -3\rangle$ d. $|R, \quad \ell = 2\rangle$ and $|L, \quad \ell = -4\rangle$. The black and red colours in (c) and (d) denote the right- and left-handedness, respectively. A linear polarizer with allows the resultant beam to interfere, producing an interferogram with various numbers of lobes. In these figures, the transmission direction of the polarizer is along the horizontal direction.

Reference

[1] L. Allen, M. W. Beijersbergen, R. J. C. Spreeuw, J. P. Woerdman, *Phys. Rev. A* **1992**, *45*, 8185.

[2] S. Baumann, D. Kalb, L. MacMillan, E. Galvez, *Opt. Express* **2009**, *17*, 9818.

[3] E. J. Galvez, S. Khadka, W. H. Schubert, S. Nomoto, *Appl. Opt.* **2012**, *51*, 2925.

[4] a) T. Bauer, P. Banzer, E. Karimi, S. Orlov, A. Rubano, L. Marrucci, E. Santamato, R. W. Boyd, G. Leuchs, *Science* **2015**, *347*, 964; b) A. M. Beckley, T. G. Brown, M. A. Alonso, *Opt. Express* **2010**, *18*, 10777.

[5] J. Hamazaki, Y. Mineta, K. Oka, R. Morita, *Opt. Express* **2006**, *14*, 8382.